

Impact of Chemical Heterogeneity on the Accuracy of Pore Size Distributions in Disordered Solids

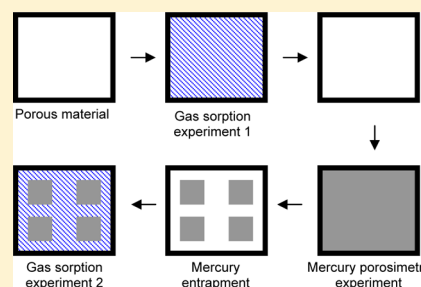
Iain Hitchcock,^{*,†} Shoaib Malik,[‡] Elizabeth M. Holt,[§] Robin S. Fletcher,[§] and Sean P. Rigby^{*,‡}

[†]Johnson Matthey Technology Centre, Blount's Court, Sonning Common, Reading, RG4 9NH, United Kingdom

[‡]Department of Chemical and Environmental Engineering, University of Nottingham, University Park, Nottingham NG7 2RD, United Kingdom

[§]Johnson Matthey Technology Centre, P.O. Box 1, Belasis Avenue, Billingham, Cleveland, TS23 1LB, United Kingdom

ABSTRACT: Disordered porous solids, such as heterogeneous catalysts, possess internal void spaces with high degrees of both chemical and geometric heterogeneity. For pore size distributions (PSDs) to be useful void space descriptors for aiding understanding of phenomena such as catalyst activity, their level of accuracy must be known. Due to differences in specific interactions and wetting behavior, the choice of adsorbate can severely impact the accuracy of PSDs derived for disordered materials using gas sorption. Wetting effects in the capillary condensation region have recently been studied extensively by simulation, but there have been no complementary, definitive experimental studies of sorption mechanisms. However, in this work, the novel integrated gas sorption and mercury porosimetry technique has been used to prepare a particular subset of pores, located within the disordered network of a given amorphous material (eg silica or alumina), that had dead-ends with different chemical properties to the walls, and then definitively compare the individual sorption behavior of two different, common adsorbates (nitrogen and argon) within just these pores. The presence of a heavy metal surface was found to lead to a shift to higher pressure in the positions of adsorption and desorption branches and a widening of the hysteresis for argon isotherms for silica pores, but not for alumina pores. In contrast, no such effect was observed for nitrogen. Hence, using argon adsorption rather than nitrogen adsorption was found likely to lead to pore size inaccuracies of at least ~200% in characterizing silica-supported platinum catalysts, for example. The experimental findings on effects of wetting and pore length were found to be consistent with findings from recent Monte Carlo and MFDFIT simulations. Further, analysis of hysteresis widths also suggested that the standard approach using NLDFT would be unsuitable for the type of samples studied here. The results highlight particular issues for the accuracy of PSDs for catalysts consisting of metal nanoparticles supported on oxide materials.



INTRODUCTION

The pore size distribution (PSD) is a widely used descriptor for the void space structure of disordered porous solids.¹ It is used to develop structural models, and understand the activity and selectivity of heterogeneous catalysts. Hence, it is essential to have an accurate PSD. Gas sorption is a very common experimental technique used to obtain the PSD. However, the algorithms used to analyze the raw sorption isotherms make a number of assumptions that impact greatly on the accuracy of PSDs, whether they are based on the Kelvin equation,¹ or nonlocal density functional theory (NLDFT).² In particular, the current standard algorithms assume that a complex, interconnected void space can be treated as a parallel pore bundle, because they assume constant pore geometry and pore-filling mechanism throughout the structure, and neglect pore–pore interactions in the condensation process. Real porous systems have pores of varying shape, length, and connectivity, as well as size, and, hence, there is also often a commensurate variation in pore-filling mechanism. In order to obtain accurate PSD information for systems with this level of complexity, the single boundary curve sorption isotherm contains insufficient information. Studies of templated porous solids only provide

detailed information on a limited range of network geometries for systems with a limited unit-cell size and are, thus, of restricted value in interpreting data for disordered solids beyond confirmation of basic theories in simple geometries, such as pore blocking in ink-bottle pores. The use of scanning curve/loop data adds to the pool of information on the void space.³ However, it has been shown recently that scanning curve/loop data is limited since these data are still a composite of the responses of many different sets of pores in the system.⁴ Hence, in order to reduce the complexity of the data analysis it is necessary to deconvolve out the behavior of different subsets of pores. This can be achieved via the integrated gas sorption and mercury porosimetry approach.⁵

The integrated gas sorption and mercury porosimetry technique^{4,5} consists of running a series of gas sorption and mercury porosimetry experiments on the same sample by freezing any entrapped mercury in-place before a subsequent gas sorption experiment. The gas sorption behavior of the pores

Received: June 3, 2014

Revised: July 28, 2014

Published: August 7, 2014

that entrap mercury can, thus, be deconvolved from the behavior of the rest using the differences in amount adsorbed between the isotherms obtained before and after mercury entrapment. This technique has been used to study the mechanisms of condensation and evaporation of nitrogen within disordered, mesoporous solids, such as confirming the presence of pore-blocking, rather than cavitation, during desorption from a disordered, mesoporous silica.⁶ Combination of the integrated method with computerized X-ray tomography of entrapped mercury allows the spatial distribution of the subset of pores isolated by the technique to be determined.⁴

Nitrogen is generally used as the adsorptive for pore characterization because it is relatively chemically inert, and is cheaply and readily available.¹ However, it is also frequently argued that argon is a better adsorptive for pore structure characterization.⁷ In particular, argon is often proposed for characterization purposes because it is nonpolar, and so it should have nonspecific interactions with the adsorbent.¹ However, argon is highly polarizable, compared to nitrogen. Further, argon has not been widely utilized in the literature because there is relatively (to nitrogen) insufficient knowledge of its adsorption behavior. For example, there is a limited amount of multilayer adsorption thickness data available,^{8–10} which means it remains difficult to correctly calculate pore sizes using the Barrett–Joyner–Halenda (BJH) approach.¹¹ Morishige and Nakamura¹² and Thommes et al.⁷ have used argon to improve the understanding of capillary hysteresis in mesoporous materials. For example, Thommes et al.⁷ have suggested comparing argon desorption isotherm NLDFT PSDs with the corresponding PSD for nitrogen to determine whether desorption is controlled by pore blocking or cavitation. Morishige and Nakamura¹² proposed that capillary condensation of argon in cylindrical pores occurs at equilibrium by studying sorption experiments at different temperatures. However, the knowledge of the sorption behavior of argon in different materials remains less than that for nitrogen.

Many of the industrial porous materials, for which gas sorption is routinely used for structural characterization, are chemically heterogeneous. Heterogeneous catalysts often consist of a physical mixture of different metal oxide materials or of metal crystallites distributed across a supposed inert support. More recently, small clusters of metal nanoparticles have been utilized by employing porous silica coatings to prevent the otherwise likely thermal sintering.¹³ The metal nanoparticle thus forms the end-walls of the dead-end of the silica pores. For all these various materials it is essential to know the mass transport accessibility of the active catalytic surface area and, hence, the pore size of the surrounding material. It is thus important to know if the chemical heterogeneity in such systems affects the accuracy of the pore size information derived from gas sorption. There have been many simulation studies of the effects of chemical heterogeneity on gas sorption. Puibasset¹⁴ compared the adsorption of argon in geometrically and chemically undulated models of cylindrical pores by introducing surface roughness parameters into solid–fluid potentials used in a mean-field interaction model for cylinders. Rasmussen et al.¹⁵ studied the influence of nonwetting defects on cavitation pressure. In particular, Do and co-workers¹⁶ have studied the influence of nonwetting patches on the shape and position of hysteresis loops for argon sorption in simple pore geometries. These workers studied the effects of increasingly nonwetting surfaces for the end-wall of dead-end pores and of varying pore length on condensation and evaporation pressures.

These simulations suggested that the determination of distributions of pore characteristic dimension (typically diameter) are complicated by other pore geometrical properties, like length, and chemical properties, like adsorbate wetting, and experimental methods to assess these effects would be beneficial to improve the accuracy of pore size distributions.

However, there are few, if any, experimental studies of the impact of chemical heterogeneity on the hysteresis loop region of isotherms in reasonably well-defined systems, as most work has focused on the multilayer region. Given that the quadrupole of nitrogen is known to interact strongly with the dipole of hydroxyl groups,¹ previous work has shown that the multilayer region adsorption of nitrogen and, hence, the BET surface area thereby obtained is affected by the degree of hydroxylation of a silica surface.¹⁷ Argon is a polarizable atom, and thus, its heat of adsorption has been used as a probe for levels of surface acidity.¹⁸ It is supposed, based on simulation studies,¹⁹ that once the surface has been covered by several monolayers of adsorbate, the effects of surface chemical heterogeneity are screened out. However, in cases of more severe chemical heterogeneity, the spatial distribution of multilayer build-up may be substantially affected.

In order to understand and determine the extent of the impact of geometrical and chemical heterogeneity on the accuracy of pore characterization of disordered solids, it is the aim of this study to compare the sorption behavior of nitrogen and argon within a particular subset of pores within materials possessing geometrically and chemically heterogeneous void space. The integrated gas sorption and mercury porosimetry technique allows the controlled introduction of chemical heterogeneity in the form of free mercury menisci of entrapped mercury. Moreover, this study will also look at the accuracy of the NLDFT algorithm for such materials. This will be achieved by using the integrated gas sorption and mercury porosimetry technique.

■ THEORY

Capillary Condensation. Capillary condensation in larger pores may be predicted by the Kelvin–Cohan equations:¹

$$\ln\left(\frac{P}{P_0}\right)_i = -\frac{k\gamma V_m \cos \theta}{RT(r_p - t_i)} \quad (1)$$

where the subscript, i , is 1 for capillary condensation and 2 for capillary evaporation, P/P_0 is the relative pressure at which condensation/evaporation occurs in a cylindrical pore of radius r_p , k is a geometry parameter and depends on the pore type (for a cylindrical pore open at both ends $k = 1$; and for a pore with one dead end, or for desorption from a hemispherical meniscus, $k = 2$), γ is the surface tension, and V_m is the molar volume of the condensed liquid phase, θ is the contact angle with which the liquid meets the wall, t_i is the adsorption film thickness, and T is the absolute temperature. It is generally assumed, for nitrogen, that the adsorbed condensate is perfectly wetting of the surface such that the contact angle is zero, and thus the $\cos \theta$ term is unity.¹ However, some studies have allowed the $\cos \theta$ term to be a free-fitting parameter,²⁰ and, by doing so, it has been shown that a corrugated, cylindrical pore geometry can give rise to all of the IUPAC standard hysteresis loop types,¹ thereby suggesting differences in pore-wetting can explain differences in isotherm shape. From eq 1, and assuming the thickness, t , of the adsorbate layer is negligible compared to the pore radius, the condensation and evaporation pressures for the

same adsorbate in open/dead-end pores of the same diameter, or identical pores with different wetting properties, can be related via

$$\left(\frac{P}{P_0}\right)_2 = \left(\frac{P}{P_0}\right)_1^n \quad (2)$$

where the exponent, n , is equal to $(k_2 \cos \theta_2)/(k_1 \cos \theta_1)$. The subscripts 1 and 2 refer to condensation and evaporation, respectively. For a through cylindrical pore with a fully wetting surface, $k_1 = 1$, $k_2 = 2$, and the $\cos \theta$ terms both equal unity. Hence, in that case, the relative pressure for evaporation is the square of the relative pressure for condensation, and so the exponent, n , is 2. For a dead-end cylindrical pore, with a fully wetting surface, $k_1 = 1$, $k_2 = 1$, and the respective $\cos \theta$ terms both equal unity. Hence, in that case, the exponent, n , will be equal to 1 and the relative pressure for evaporation will be the same as the relative pressure for condensation. If the adsorbate–adsorbent interaction becomes more nonwetting for capillary condensation than for evaporation, the exponent, n , will increase. Moreover, eq 2 predicts that as the adsorbate–adsorbent interaction becomes more nonwetting for capillary condensation the width of hysteresis will increase.

A more sophisticated approach to multilayer adsorption was developed by Broeckhoff and de Boer,^{21,22} which related the thickness of the adsorbed layer to the pore curvature and relative pressure. Their work found the exponent value in eq 2 was 1.5 for nitrogen in a through cylindrical pore. The exponent value will be tested in this paper.

Surface Wetting. In order to assess the degree of wetting of the overall internal surface of the sample by an adsorbate, a similar approach to that introduced by Pfeiffer et al.²³ to study adsorption on precoated surface films will be used. This method has also, subsequently, been used to determine the spatial distribution of polymer within silica pores.²⁴ The method compares the fractal dimension, obtained via gas adsorption, before and after adding another substance to a porous solid. For preadsorbed films on rough surfaces, the fractal dimension may decrease if the film preferentially fills concavities, thereby smoothing out the perceived surface.²³ Where the added substance does not wet the surface, but remains in isolated ganglia, the measured fractal dimension will remain (virtually) unchanged because the new surface from the added substance will be small and a substantial fraction of the original rough surface remains exposed.²⁴ For the samples considered here, previous SAXS and adsorption studies have shown that the internal surfaces are very rough.²⁵ It is expected that when mercury becomes entrapped within the pore network, its nonwetting nature will mean it will tend to reduce its external surface area and, hence, to form ganglia with smooth external surfaces. If a large number of these smooth surfaces of mercury ganglia are accessible to the adsorbate, then this will mean that the previously accessible rough surface of the region of void space now blocked off by mercury will be replaced by the smoother surface of the mercury ganglia. Hence, in this case, it is anticipated that the apparent overall roughness of the internal sample surface should decline on mercury entrapment. However, if the adsorbate tends not to wet the mercury surface, and thence adsorb predominantly on the remaining rough oxide surfaces, then the degree of surface roughness perceived by the nonwetting adsorbate will not decline, as it will only “sample” the rough surface. It is thus expected that, for an adsorbate that wets mercury, the measured

surface fractal dimension will decline following mercury entrapment, while it will not decline for nonwetting adsorbates.

The analysis method used to derive surface fractal dimensions from gas adsorption data was the fractal version of the BET theory. The derivation^{26,27} of a fractal BET equation is based upon the fact that, for a fractal surface, the area available for adsorption in the i th layer of adsorptive decreases by a factor f_i , given by

$$f_i = \frac{A_i}{A_1} = i^{\alpha-1} \quad (3)$$

where $\alpha = 3 - d$, from that (A_1) which is available for the adsorption of the initial monolayer. Mahnke and Mögel²⁷ suggested an alternative derivation of a fractal BET equation to that initially proposed by Fripiat et al.²⁶ The alternate derivation avoids the inconsistent behavior, for the earlier equation, in the case of a surface fractal dimension of 3. The isotherm equation derived by Mahnke and Mögel²⁷ is given by

$$\log[V_{(P/P_0)}] = \log(V_m) + \log\left[\frac{C(P/P_0)}{1 - (P/P_0) + C(P/P_0)}\right] - (3 - d)\log[1 - (P/P_0)] \quad (4)$$

where V is the volume adsorbed, V_m the monolayer volume, C is the fractal BET constant, P/P_0 is the relative pressure, and d is the fractal dimension. Equation 4 was fitted between relative pressures 0.05–0.6 for all isotherms before and after mercury porosimetry. This pressure range includes the typical range of validity of the standard BET equation (~ 0.05 to ~ 0.35) but is expanded at the high pressure end to include more of the multilayer adsorption region where the fractal-dependent behavior becomes more apparent, while avoiding the capillary condensation region for which the BET theory is not appropriate.

An alternate method to derive a fractal dimension is to use the Frenkel–Halsey–Hill equation (FHH).¹ The FHH equation is strictly valid only above monolayer coverage. This means the fractal BET equation works over a wider pressure range in the multilayer region and, thus, has been used in this study. Having said that, we have previously shown that the fractal dimension derived using the FHH and BET equations are similar for nitrogen (77 K) on silica samples.¹⁷

■ EXPERIMENTAL SECTION

Samples Studied. The materials studied in this work were two commercially available sol–gel silica spheres, denoted S1 and G1, and a commercially available alumina extrudate, denoted E2. The pore structures of the as-received materials have been characterized in detail in earlier work.^{4–6,25} All of the samples are unimodal, mesoporous materials.

Integrated Gas Sorption and Mercury Porosimetry Experiments. Nitrogen sorption experiments were performed at 77 K by use of a Micromeritics Accelerated Surface Area and Porosimetry (ASAP) 2020 apparatus. The sample was placed into a preweighed Micromeritics gas sorption tube, and a seal frit was placed at the top. The seal frit had two functions. It first prevented any sample being evacuated into the manifold of the Micromeritics ASAP apparatus. Second, it allowed the Micromeritics gas sorption tube to be removed from the Micromeritics ASAP 2020 apparatus, but keeping the sample inside enclosed in an inert atmosphere of nitrogen. The sample tube (with sample) was attached to the ASAP 2020 and heat treated

under vacuum to remove any physisorbed gases. The heat treatment involved heating the sample to 90 °C under a virtual vacuum (1×10^{-5} mmHg) to first remove any physisorbed water. The temperature was then increased to 150 °C and the sample was left for 12 h. After the heat treatment, the sample tube was removed from the ASAP 2020 (seal frit attached) to calculate the dry sample mass. A Micromeritics patented isothermal jacket was then placed around the sample tube and it was reattached to the ASAP 2020. The isothermal jacket ensured a constant thermal profile of 77 K along the length of the sample during the analysis. The gas sorption experiment was fully automated, and the relative pressures studied were between 0.004–1.00. At each pressure point the saturation pressure was calculated in a cell, which was adjacent to the sample. The gas sorption experiment works by dosing an amount of gas, into a fixed volume chamber where the sample (the adsorbent) is situated. The sample, over a period of time, adsorbs the gas and eventually the adsorbed gas (the adsorbate) reaches an equilibrium state with the gas phase. At this point, the Micromeritics equipment calculates the amount of gas that has been adsorbed onto the sample and then doses another amount of gas. The time it takes for the adsorbed gas and the bulk gas to reach equilibrium with one another depends on the adsorbent, the adsorbate, the temperature and the pressure. This period of time can be found by studying the gas sorption isotherm at two different equilibration times. If the amount of adsorbed gas, at a specific pressure, is the same for both times, the system must have reached equilibrium by the shortest time used. If the amount of adsorbed gas is not the same for the two different times used, then it cannot be said that the system is at equilibrium for either of the times. In which case, the experiment would need to be repeated with longer time scales until the amount adsorbed remains unchanged, thus confirming equilibration. The equilibration time used in these studies was tested and found to be 25 s.

Following the gas sorption experiment, the sample tube was allowed to reach ambient temperature (~ 293 K), and the sample was then transferred to a Micromeritics mercury penetrometer. The transfer took place in a small glovebox, which was under a dry nitrogen atmosphere. This minimized any adsorption of water from the atmosphere onto the sample when the transfer between sample tubes took place. A mercury porosimetry experiment was then performed using a Micromeritics Autopore IV 9450 apparatus. The sample was first evacuated to 6.7 Pa to remove physisorbed water that had adsorbed onto the sample when it was transferred from the gas sorption apparatus. When the system was at vacuum, mercury was allowed to enter the penetrometer and then the pressure was increased toward ambient. The penetrometer was then transferred to a pressure vessel that could reach a maximum pressure of 414 MPa. A fully automated mercury porosimetry experiment was then studied from ambient pressure to 414 MPa using a standard 15 s equilibration time between pressure steps.

Following the mercury porosimetry experiment, the sample (and mercury) was transferred to a fume cupboard and placed in a crucible. Using tweezers, the sample was removed from the mercury and transferred back into the Micromeritics gas sorption tube. The gas sorption tube was reattached to the Micromeritics ASAP 2020 and a filled liquid nitrogen Dewar was raised around the tube to cool the system to 77 K. This set up was left for 30 min to ensure all the mercury inside the sample became frozen, before the system was then evacuated to

start the next nitrogen sorption experiment. If the mercury was not frozen, a potential hazard would be introduced, as the vacuum pump used to evacuate the sample at the beginning of the gas sorption experiment was vented into the laboratory.

Argon sorption at 87 K was also studied. The integrated experiment was as follows: (1) Nitrogen sorption experiment at 77 K; (2) Argon sorption experiment at 87 K; (3) Mercury porosimetry experiment; (4) Nitrogen sorption experiment at 77 K; (5) Argon sorption experiment at 87 K.

This procedure was also studied with the order of steps 1–2 and 4–5 reversed, with the reason for this change as follows. When the sample was transferred from the mercury porosimeter to the gas sorption apparatus, the protection from exposure to atmospheric moisture was not completely perfect, and so the sample could have potentially adsorbed some water from the atmosphere. This adsorbed water could not be removed by heating the sample under vacuum (for safety reasons) as there was then mercury in the sample. Therefore, when the sample was subsequently studied by nitrogen sorption, any adsorbed water would freeze when the sample was cooled to 77 K. Due to the thermal expansion of water on freezing, this freezing process might have caused the sample to crack, thereby generating larger pores, but this would be undetectable in the first freezing step with the water ice still in place. However, following the nitrogen experiment, the adsorbed water can subsequently thaw and potentially move out of any cracks. To check that this did not occur, experiments were conducted where the argon isotherms were obtained before the nitrogen isotherms and vice versa. In the former case, this would eliminate the freeze–thaw mechanism before the argon gas sorption experiment and, in the latter, before the nitrogen sorption experiment. Comparing the integrated gas sorption–mercury porosimetry–gas sorption experimental results for the data sets where the nitrogen and argon isotherms were obtained in alternate orders, no difference was observed. This suggested that water penetration and freezing was not a problem.

■ RESULTS AND DISCUSSION

Fractal Analysis of Multilayer Region of Adsorption Isotherms. The surface fractal dimensions derived, using the fractal BET eq 4, from gas adsorption isotherms obtained before and after mercury porosimetry are presented in Table 1.

From Table 1, it can be seen that there were significant differences between the fractal dimensions obtained before and after mercury porosimetry using nitrogen adsorption on all samples and also for argon on sample E2, but there was no significant difference in the equivalent pairs of fractal dimensions obtained using argon adsorption on the silica samples G1 and S1. Further, the surface fractal dimensions have also been independently obtained previously from SAXS for samples G1 and S1^{17,25} and are 2.27 ± 0.11 and 2.31 ± 0.04 , respectively. It can be seen that, while the fractal dimensions obtained from argon adsorption for these same materials are very similar to those obtained by SAXS, those obtained by nitrogen adsorption are significantly higher than obtained by SAXS. The reasons for the discrepancy between fractal dimensions obtained from nitrogen adsorption and SAXS have been studied in earlier work, and it was attributed to the specific interactions between the nitrogen quadrupole and the dipoles of surface hydroxyl groups of silicas.¹⁷ The similarity of the fractal dimension from argon adsorption on G1 and S1 following mercury entrapment to that obtained from SAXS

Table 1. Sample Mean Surface Fractal Dimensions Determined from Either (a) Nitrogen or (b) Argon Adsorption before and after Mercury Porosimetry Using Eq 4^a

(a)		
sample	fractal dimension	
	before mercury porosimetry	after mercury porosimetry
S1	2.46 ± 0.01	2.29 ± 0.01
G1	2.38 ± 0.01	2.27 ± 0.01
E2	2.302 ± 0.001	2.135 ± 0.005
(b)		
sample	fractal dimension	
	before mercury porosimetry	after mercury porosimetry
S1	2.32 ± 0.01	2.31 ± 0.01
G1	2.25 ± 0.01	2.23 ± 0.01
E2	2.27 ± 0.01	2.19 ± 0.01

^aQuoted errors are one standard error.

suggests that the experimental procedure does not result in water contamination, as any potential adsorbed water film would be expected to alter the fractal dimension perceived by argon. Further, this very close similarity in the surface fractal dimensions, obtained from argon adsorption, before and after mercury entrapment in G1 and S1 also suggests that the differences seen in the other experiments cannot be due to just water contamination during the experimental procedure, because this would have been expected to have impacted the data for all samples, including G1 and S1, as the procedures were the same for all. In addition, for G1 and S1, the percentage drop in the monolayer volume for argon, before and after mercury porosimetry, was larger than it was for nitrogen.

Sample S1 Capillary Condensation Region. Integrated Nitrogen Sorption and Mercury Porosimetry Experiments. The gas sorption isotherm data obtained before mercury porosimetry were analyzed by calculating the change in the amount adsorbed between each pressure point. This procedure was then repeated on the gas sorption isotherm following mercury porosimetry. Finally, the change in volume between two pressures following mercury porosimetry is subtracted from the change in volume between the same two pressures before mercury porosimetry. This change in incremental amount adsorbed can then be plotted against pressure. Typical examples of the adsorption and desorption change in incremental amount adsorbed plots for nitrogen in S1 are shown in Figure 1. An inset shows the hysteresis loop region of the nitrogen gas sorption isotherm before and after mercury porosimetry on S1. The area and shape of the positive deviations are approximately the same for the adsorption and desorption plots. The only difference appears to be that the adsorption change in incremental amount adsorbed plot is shifted to higher relative pressures. This is expected because $P_{\text{adsorption}} > P_{\text{desorption}}$ where P is pressure. As discussed previously,⁴ the similar shapes would indicate that the pores which entrap mercury fill and empty like independent pores, and this can be confirmed using a counter example. The counter example assumes that the pores which entrap mercury capillary fill as independent pores, but the pores empty by a pore blocking mechanism. If this was the case, it would be anticipated that the desorption process would occur over a narrower pressure range. As will be seen below, experimentally this is not what was observed, and, therefore, it must be that the

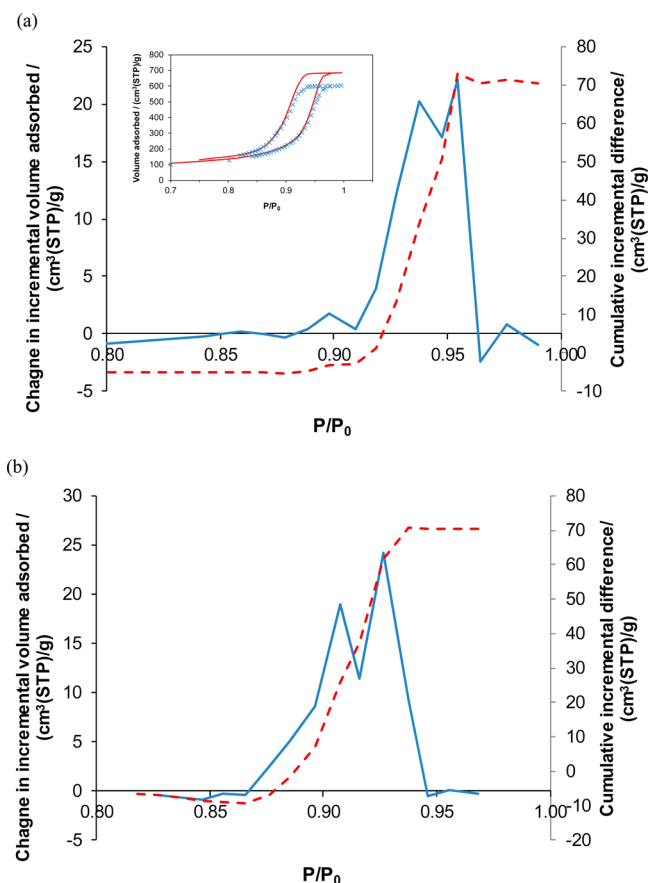


Figure 1. (a) Adsorption (solid line; left axis) change in incremental amount adsorbed plot, for N₂ adsorption at 77 K on S1. Overlaid is the cumulative incremental amount difference plot (dashed line; right axis). Inset is the hysteresis loop region of the nitrogen gas sorption isotherm before (solid line) and after (crosses) mercury porosimetry on S1. (b) Desorption (solid line; left axis) change in incremental amount adsorbed plot, for N₂ at 77 K on S1. Overlaid is the cumulative incremental amount difference plot (dashed line; right axis).

adsorption and desorption processes, in the pores that entrap mercury, capillary fill and empty like independent (open) cylindrical pores. Also shown in Figure 1 are the cumulative incremental difference plots. While making the direction of the change in amount adsorbed following mercury easier to visualize, being, in effect, histograms, the shapes of the incremental plots are potentially sensitive to the particular choice of pressure points measured. However, the overall shape of the cumulative plots is not affected by this choice, and the effects of random error are also reduced toward the high pressure end. The cumulative plots lead to the same conclusions as the incremental plots, about the direction of the change in the amount adsorbed over a given pressure range, and thus, the choice of pressure points was not significant. It can be seen that the form of the cumulative plots is roughly the same for both adsorption and desorption in S1 and consists of a relatively flat region at low relative pressure, followed by a steep rise, and then another relatively flat plateau at high relative pressure.

Implicit in the Kelvin-Cohan equations for a through,²⁸ cylindrical pore is the concept that, upon adsorption in an open cylindrical pore, gas adsorbs on the pore wall in a thin film (cylindrical meniscus), and then this film becomes unstable and

the whole pore fills with condensate. Desorption, however, can occur from both ends of the pore via hemispherical menisci. Due to the difference in the menisci geometries for adsorption and desorption, the relationship between the adsorption and desorption relative pressures, is given as

$$\left(\frac{P_{\text{desorption}}}{P_0}\right) = \left(\frac{P_{\text{adsorption}}}{P_0}\right)^2 \quad (5)$$

This relationship may also hold true for a through ink-bottle pore geometry, and this is explained as follows. For a through (open) ink-bottle pore geometry, if the radius of the two shielding pore necks is greater than half that of the intermediate pore body, then all pores will fill at the same pressure. This is because once condensate has filled the pore necks, filling of the pore body may then proceed via ingress of the, now hemispherical, meniscus from the end of the pore necks. The ink-bottle pore geometry will also empty at a single pressure due to the pore blocking mechanism. In this case the pressure required to capillary fill, and empty, the ink-bottle pore is equivalent to that given by the Kelvin-Cohan equation for a cylindrical, and hemispherical meniscus in the pore neck. Therefore, this through ink-bottle pore geometry would appear to behave like an independent through pore. In such a case the geometric configuration of the adsorbate would be identical at the same amount adsorbed on both the adsorption and the desorption branches of the isotherm, as has been observed by NMR relaxometry for water adsorption on silicas (although not attributed to this effect at the time).²⁹

In previous studies, Perkins et al.³⁰ have demonstrated, using NMR cryoporometry, that the pores in **S1** are cylindrical in shape. Moreover, in our previous paper we showed that the pores that entrap mercury capillary fill and empty like independent through pores since pore necks control both capillary condensation and evaporation.⁴ Therefore, the relationship in eq 5 can be tested using the pores in **S1** that entrap mercury. This test has been carried out using the following method. All of the pressures in the adsorption change in incremental amount adsorbed plot (closed diamonds in Figure 1) have been squared and the resultant plot has been overlaid with the desorption change in incremental amount adsorbed plot (Figure 2a).

It can be seen in Figure 2a that the adsorption change in incremental amount adsorbed plot now becomes shifted to lower relative pressures compared to the analogous desorption plot. This indicates that the width of hysteresis in the pores which entrap mercury was narrower than what is predicted by the Kelvin-Cohan equations for fully wetting, through cylindrical pores. Empirically, it has been found, by the process of trial and error, that the relationship between the adsorption and the desorption relative pressures, in the pores which entrap mercury, can be expressed by

$$\left(\frac{P_{\text{desorption}}}{P_0}\right) = \left(\frac{P_{\text{adsorption}}}{P_0}\right)^{1.5} \quad (6)$$

This relationship is demonstrated in Figure 2b, which shows the adsorption change in incremental amount adsorbed plot overlaying the desorption plot. Although the exponent is the same as what was predicted by Broekhoff and de Boer for nitrogen in a through cylindrical pore, we are not concluding that this theory is correct. It is clear, however, that the Kelvin-Cohan prediction is incorrect for **S1**.

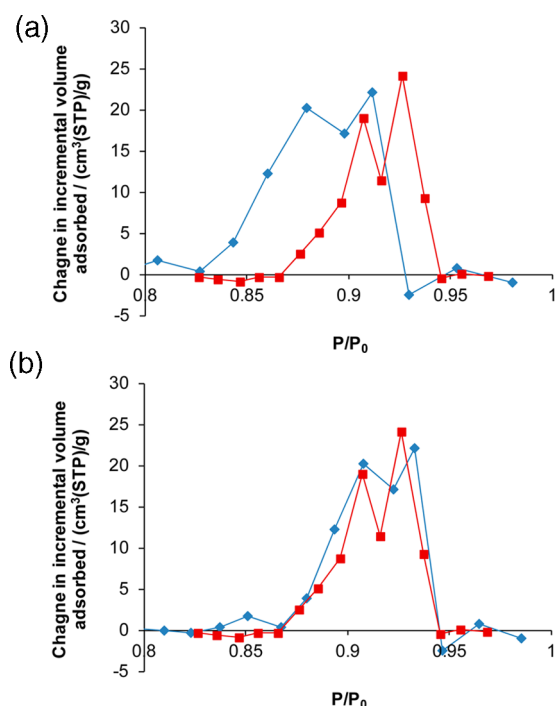


Figure 2. (a) Adsorption (closed diamonds) change in incremental amount adsorbed plot, for N₂ at 77 K on **S1**, where all relative pressures have been squared. The desorption (closed squares) change in incremental amount adsorbed plot is the same as in Figure 1. Lines have been added to guide the eye. (b) Adsorption (closed diamonds) change in incremental amount adsorbed plot, for N₂ at 77 K on **S1**, where all relative pressures have been raised to the power 1.5. The desorption (closed squares) change in incremental amount adsorbed plot is the same as for Figure 1. Lines have been added to guide the eye.

The reason for this may be because it has been suggested that the Kelvin-Cohan equations do not correctly predict the capillary condensation and evaporation processes in pores less than ~20 nm in diameter.² This is because the Kelvin-Cohan equations are based on macroscopic properties such as the surface tension and contact angle between the liquid meniscus and the pore wall. It is believed that these assumptions are inappropriate for pores less than ~20 nm in diameter. Due to this, studies by Neimark and Ravikovitch² advocate the use of DFT to calculate the size of cylindrical pores from experimental gas sorption studies. This is because DFT provides a microscopic model of the gas sorption process taking into account gas–gas, gas–liquid, gas–solid, and liquid–solid interactions as well as the pore geometry. To verify their theoretical approach, they have compared their studies to experimental gas sorption experiments using templated mesoporous materials such as MCM-41 and SBA-15.² They report that there is a quantitative agreement between the theoretical isotherms, using DFT, and the experimental studies. This would suggest that the DFT method can be used to correctly predict pore sizes from experimental gas sorption studies. However, there is an inherent problem with their method to check the theoretical approach, which is explained as follows. All their experimental studies use MCM-41, SBA-15, and other materials that have pore sizes such that capillary condensation and evaporation occur in the relative pressure range ~0.4–0.7. The DFT calculations have not been compared to experimental data for larger pores where capillary

condensation and evaporation happens above relative pressure 0.7. This is because there are no templated materials with pores that capillary fill and empty at these high relative pressures. Therefore, there is some doubt about the DFT method to calculate pore sizes for systems where capillary hysteresis happens above relative pressure ~ 0.7 . It is important to verify the DFT method above relative pressure 0.7. This is because many industrial catalyst support materials have pores such that capillary condensation of nitrogen at 77 K occurs above relative pressure 0.7. As mentioned above, the pores that entrap mercury in **S1** capillary fill and empty like independent pores. Moreover, capillary condensation and evaporation in these pores happens above a relative pressure of 0.85. This means that **S1** has suitably sized pores that can test the DFT calculations at relative pressures higher than ~ 0.7 . Further, for the DFT simulation, the interaction strength between nitrogen and a silica surface is determined by adjusting the simulation parameter until there is good agreement between the experimental isotherm for adsorption upon a standard, nonporous silica (Aerosil), and the corresponding DFT simulated isotherm.³¹ The accuracy of the DFT predictions thus relies on the appropriateness of the calibration standard surface to represent other silica surfaces.

Neimark and Ravikovitch² have calculated, using DFT, the adsorption and desorption isotherms in cylindrical pores of sizes 2–100 nm. In their studies they have plotted the capillary condensation relative pressures and capillary evaporation relative pressures for the different pore sizes. These data are shown in Figure 3a. The closed diamonds represent the capillary condensation transitions for the different size pores and the open squares represent the corresponding capillary evaporation transitions. Figure 3b shows an enlarged area of Figure 3a, between relative pressures 0.85–1. By a process of trial and error, the width of the hysteresis predicted by DFT has been tested. It has been found that the relationship between the adsorption relative pressures and desorption relative pressures, between relative pressures 0.85–1, can be expressed by

$$\left(\frac{P_{\text{desorption}}}{P_0}\right) = \left(\frac{P_{\text{adsorption}}}{P_0}\right)^{1.8} \quad (7)$$

This relationship is shown by the solid line in Figure 3b. This means that the width of hysteresis predicted by DFT in cylindrical pores is narrower than predicted by the Kelvin-Cohan equations. However, the width of hysteresis predicted by DFT is wider than found experimentally for the pores in **S1** that entrap mercury. If the width of hysteresis in **S1** was determined by a pore blocking mechanism, it would be anticipated that the hysteresis width would be wider than that predicted by DFT. Experimentally, as stated, it has been found that the hysteresis is, instead, narrower for **S1**. This suggests that DFT does not correctly predict the adsorption and desorption processes in silica **S1**. The discrepancy may be due to a difference in wetting properties of the **S1** surface and the reference silica used to calibrate the interaction parameters in NLDFT. This is the first time that experimental data has been used to test DFT calculations in pores that capillary fill and empty above relative pressure ~ 0.7 .

Furthermore, using the adsorption and desorption change in incremental amount adsorbed plots the adsorption and desorption boundary curves, for the pores which entrap mercury in **S1**, can be generated. This is done by cumulatively adding the adsorption change in incremental amount adsorbed,

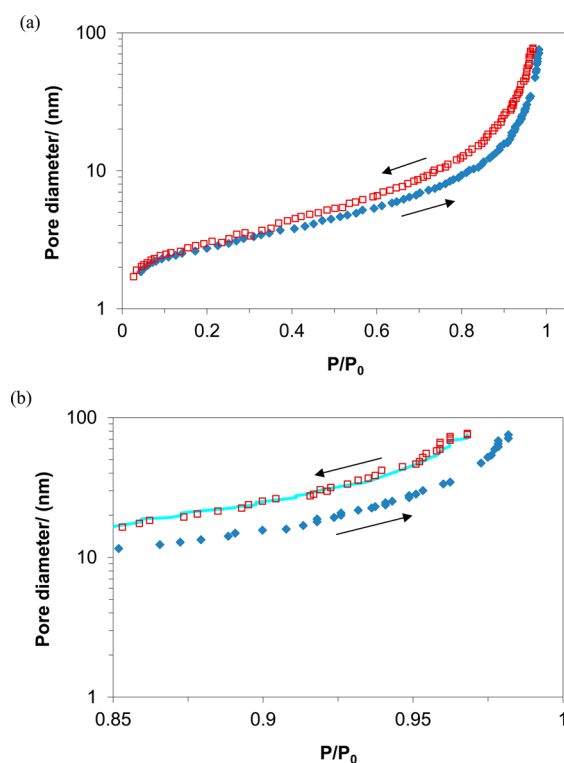


Figure 3. (a) Data is from Neimark and Ravikovitch:² Capillary hysteresis of N_2 in cylindrical pores at 77 K. The closed diamonds show the spinodal condensation pressure and the open squares the equilibrium desorption pressure. Arrows have been added to show the direction of the change in pressure. (b) Enlarged region of Figure 3a. The solid line represents the relationship in eq 7. Arrows indicate the direction of the change in pressure.

or by cumulatively subtracting the desorption change in the incremental amount adsorbed, for the adsorption and desorption curves, respectively. The adsorption and desorption boundary curves for the pores which entrap mercury are shown in Figure 4. The hysteresis loop is of Type H1, since the adsorption and desorption boundary curves are parallel. This is expected for a system that is made up of independent (open) cylindrical pores, or a system with open ink-bottle pores (as discussed above). Furthermore, for a system with Type H1 hysteresis the adsorption and desorption scanning curves

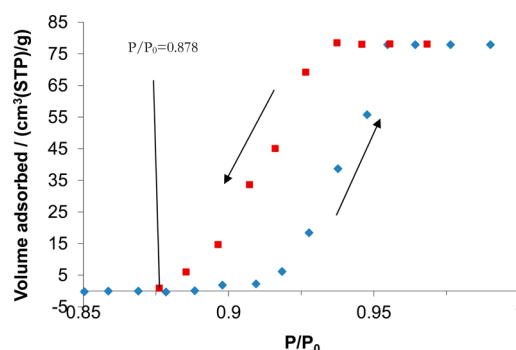


Figure 4. Adsorption (closed diamonds) and the desorption (closed squares) boundary curves for the pores that entrap mercury for **S1**. The arrows have been added to indicate the direction of the change in pressure.

should cross directly between the boundary curves. We have shown this to be the case in our previous studies.⁴

Argon Sorption–Mercury Porosimetry–Argon Sorption Experiments. A typical example of a set of argon sorption isotherms (between relative pressures 0.6–1) obtained for **S1** before and after mercury was entrapped is shown in Figure 5. It

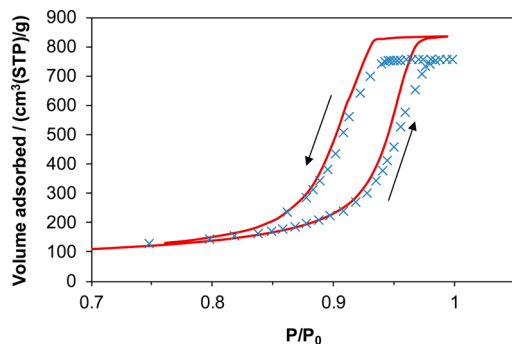


Figure 5. Hysteresis loop region of the argon 87 K gas sorption isotherm before (solid line) and after (crosses) mercury porosimetry on **S1**. Arrows have been added to indicate the direction of the change in pressure.

is noted that the shape of the hysteresis loop is similar to the analogous set of nitrogen isotherms for **S1**.⁴ This suggests that the capillary condensation and evaporation mechanisms appear similar for both adsorbates.

The adsorption and desorption change in incremental amount adsorbed plots for argon are shown in Figure 6. The series of changes in increments for each pressure have also been added sequentially to produce a cumulative incremental amount adsorbed plot. Both types of plots are shown in Figure 6 for a typical integrated argon sorption experiment. The adsorption change in incremental amount adsorbed plot is explained as follows. Between relative pressures of 0.913 and 0.954 there is a positive peak. At a relative pressure of 0.959 the incremental amount adsorbed becomes negative, which contrasts with the analogous nitrogen plot (see Figure 1). The desorption change in incremental amount adsorbed plot is of similar form to the adsorption plot and is explained as follows. At relative pressure 0.933 there is a negative signal, and as the pressure is lowered, the signal becomes positive (relative pressure 0.922). The signal remains positive until relative pressure 0.872. The negative signal indicates that, following the mercury porosimetry experiment, there are now some pores that, while remaining externally accessible, now fill at a higher relative pressure. The substantial decline in the cumulative incremental difference plot, at high relative pressures following the steep rise, for argon adsorption or desorption contrasts with the flat plateau at high relative pressure of the cumulative plot for nitrogen in Figure 1.

In order to study changes to the width of the hysteresis with mercury entrapment, the relative pressures for the adsorption change in incremental amounts adsorbed were, in turn, raised to powers of 1.5 and 1.9, and the modified plots compared with the corresponding data for the desorption isotherms in Figure 7. It can be seen that raising the relative pressures for the adsorption data to a power of 1.5 leads to a good overlap of the low pressure flank of the positive peak. However, it can be seen that raising the adsorption data relative pressures to a power of 1.9 leads to a good coincidence of the negative peak with that for desorption. The pores represented by the negative peak are

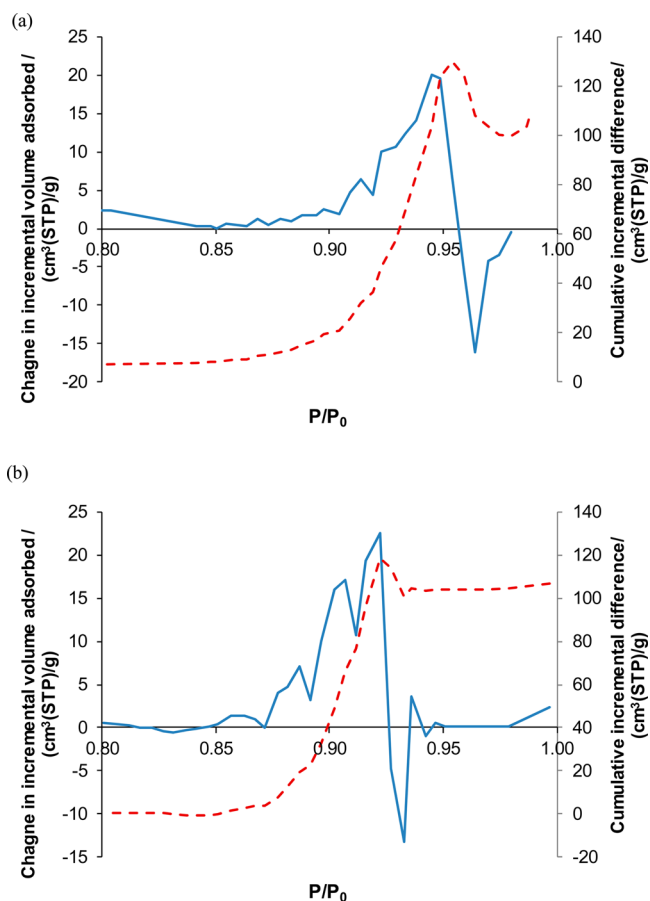


Figure 6. (a) Adsorption (solid line; left axis) change in incremental amount adsorbed plot, for Ar at 87 K on **S1**. Overlaid is the cumulative incremental amount difference plot (dashed line; right axis) (b) Desorption (solid line; left axis) change in incremental amount adsorbed plot, for Ar at 87 K on **S1**. Overlaid is the cumulative incremental amount difference plot (dashed line; right axis).

affected by mercury entrapment but not occupied by mercury. The pores represented by the majority of the positive peak are those pores that fill completely with mercury. The similarity of the power that leads to superposition of the nitrogen adsorption and desorption data, and the low pressure flank of the adsorption and desorption data for argon suggests that, for all pores before mercury entrapment, the width of the argon hysteresis is similar to that for nitrogen. However, after mercury entrapment, the presence of mercury affects the condensation and evaporation pressures, and the width of hysteresis for argon only for some pores that remain accessible. As discussed in the Experimental Section, the order of the nitrogen and argon sorption experiments was reversed and there was no difference in the argon and nitrogen change in incremental amount adsorbed plots. Therefore, the negative peak in the argon change in incremental amount adsorbed plot could not have been caused by an artifact of the experiment.

Sample G1. Figure 8 shows typical examples of incremental amount adsorbed plots and of cumulative incremental difference plots for nitrogen adsorption and desorption on **G1**. The overall form of the adsorption/desorption change in incremental amount adsorbed plots for **G1** is similar to **S1** in that it is dominated by a large positive peak and little, or no, negative deviation at higher relative pressures beyond the positive peak. However, the data for **G1** does include more

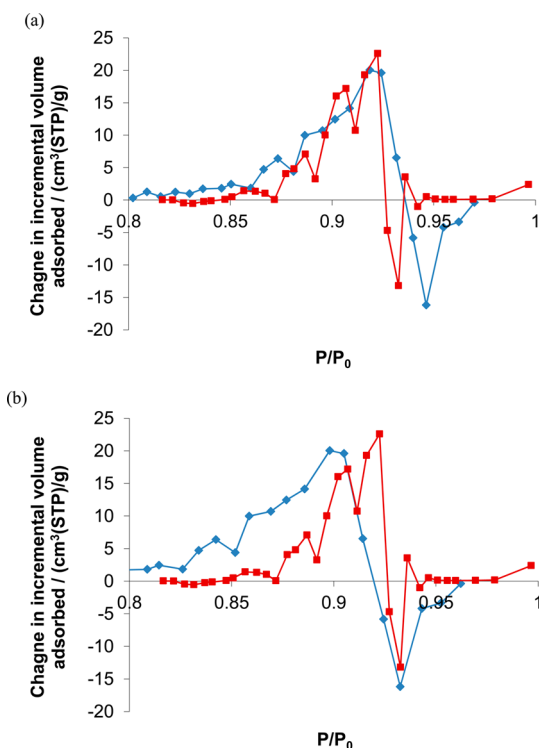


Figure 7. Adsorption (closed diamonds) change in incremental amount adsorbed plot, for argon at 87 K on **S1**, where all relative pressures have raised to the power 1.5 (a), and 1.9 (b). The desorption (closed squares) change in incremental amount adsorbed plot for argon at 87 K on **S1**. Lines have been added to guide the eye.

significant negative deviations at relative pressures lower than the positive peak. This suggests that, following mercury entrapment, some pores are filling and emptying at lower relative pressure than before. The significance of this finding will be explained below.

Figure 9 shows typical examples of incremental amount adsorbed plots and of cumulative incremental difference plots for argon sorption on **G1**. It is noted that the form of these plots for argon is significantly different to those for nitrogen. The form of the adsorption/desorption change in incremental amount adsorbed plots for argon on **G1** is similar to **S1**. For the adsorption plot, between relative pressures of 0.839 and 0.919, there is a positive peak. At a relative pressure of 0.934, the incremental amount adsorbed becomes negative. The desorption change in incremental amount adsorbed plot is of similar form to the adsorption plot and is explained as follows. At relative pressure 0.852 there is a negative signal and as the pressure is lowered the signal becomes positive (relative pressure 0.821). The signal remains positive until relative pressure 0.794. Like **S1**, the negative signal indicates that, following the mercury porosimetry experiment, there are then some pores that, while remaining externally accessible, now fill at a higher relative pressure. It is also noted that to superpose the negative high pressure peaks of the incremental difference plots for adsorption and desorption of argon on **G1** required the relative pressures for the adsorption data to be raised to a higher power than it does to superpose the large positive peaks.

Sample E2. Figure 10 shows typical examples of incremental amount adsorbed plots and of cumulative incremental difference plots for nitrogen adsorption and desorption on **E2**. The form of the adsorption/desorption

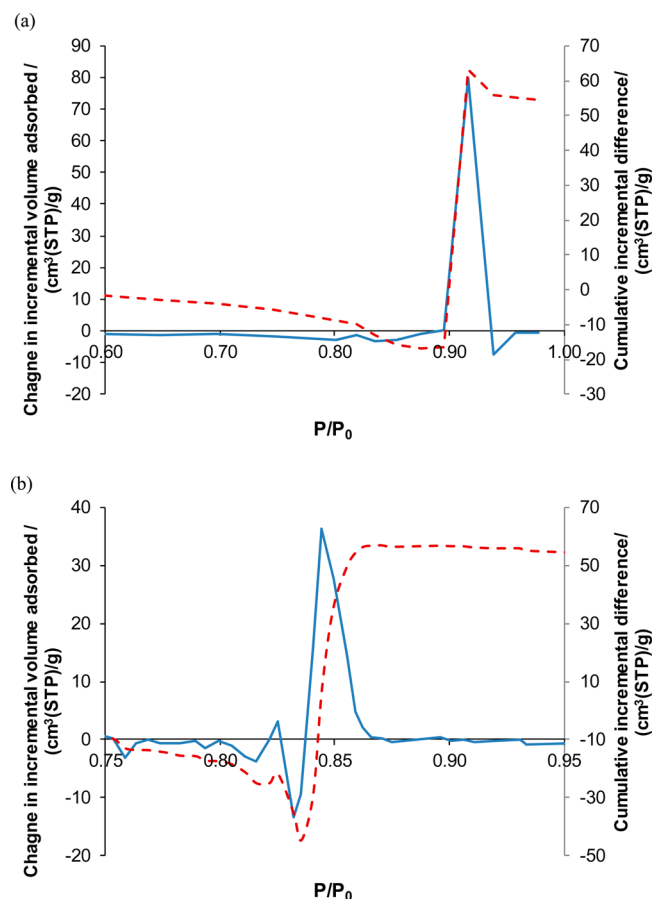


Figure 8. Change in incremental volume adsorbed (between before and after mercury entrapment) plot (solid line; left axis) and cumulative incremental difference plot (dashed line; right axis) for adsorption (a) and desorption (b) of nitrogen on a typical sample from batch **G1**.

change in incremental amount adsorbed plots for nitrogen on **E2** are similar in form to those for **S1** and **G1** since there are no substantial negative peaks at higher relative pressure than the large positive peak. The cumulative incremental difference plot for nitrogen adsorption on **E2** is similar to those for **S1** and **G1**, in that following the steep rise there is a relatively flat plateau at high relative pressure. The cumulative incremental difference plot for nitrogen desorption from **E2** is similar to that for **G1**, in that there is a negative peak at low relative pressures before the steep rise followed by a relatively flat plateau at the highest relative pressures.

Figure 11 shows typical examples of incremental amount adsorbed plots, and of cumulative incremental difference plots, for argon adsorption and desorption on **E2**. The form of the adsorption/desorption change in incremental amount adsorbed plots for argon on **E2** are unlike those for **S1** and **G1** since there are no substantial negative peaks at higher relative pressure than the large positive peak. Therefore, the negative signal in the change in incremental amount adsorbed plots for argon (87 K) must be dependent on the nature of the sample. **S1** and **G1** are sol-gel silicas, while **E2** is an alumina. The cumulative incremental difference plots for argon adsorption and desorption both have a relatively flat plateau at the highest relative pressures.

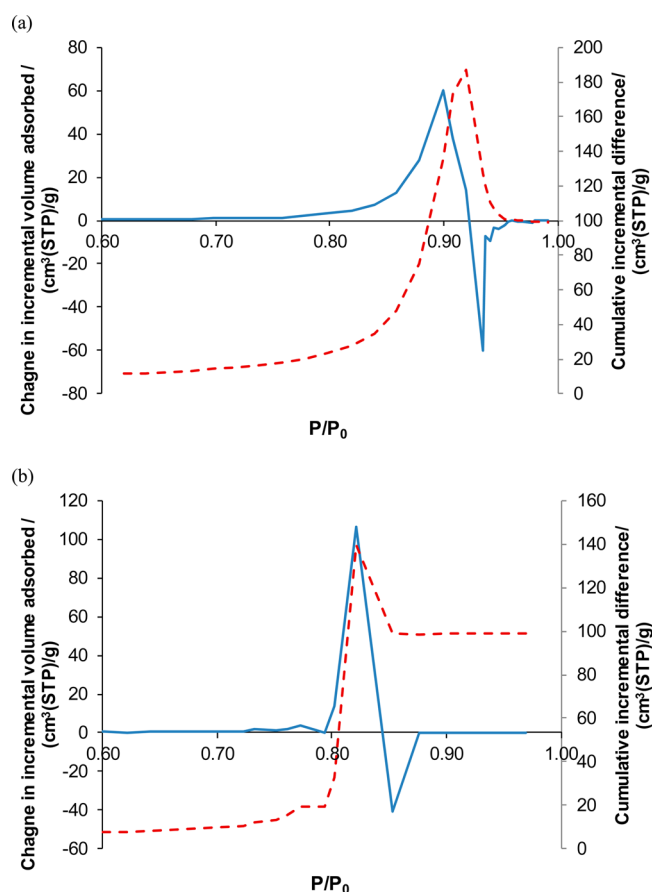


Figure 9. Change in incremental volume adsorbed (between before and after mercury entrapment) plot (solid line; left axis) and cumulative incremental difference plot (dashed line; right axis) for adsorption (a) and desorption (b) of argon on a typical sample from batch G1.

DISCUSSION

It has been observed that the surface fractal dimension measured using nitrogen adsorption declines significantly following mercury entrapment in all of the samples studied, and for argon adsorption on the alumina sample. However, the surface fractal dimension does not decline significantly following mercury entrapment for argon adsorption in the sol-gel silica samples and remains similar to that obtained from SAXS. These findings suggest that argon does not substantially wet any exposed mercury surfaces in the sol-gel silicas up to at least relative pressure 0.6. Given that the surface fractal dimension does decline for nitrogen for the silicas, this suggests that significant numbers of new menisci of entrapped mercury are accessible to adsorbing gas. Hence, this suggests that the mercury surfaces are relatively nonwetting for argon adsorption relative to silica. This wetting theory is supported by the fact that the % monolayer volume drop for argon sorption on G1 and S1, before and after mercury porosimetry, was greater than the corresponding percentage monolayer volume change for nitrogen. However, the decline in fractal dimension following mercury entrapment for argon adsorption on E2 suggests that the mercury surface is wetting for argon relative to an alumina surface. The difference in adsorption behavior between silica and alumina may reflect the difference in surface chemistry between silica and alumina.

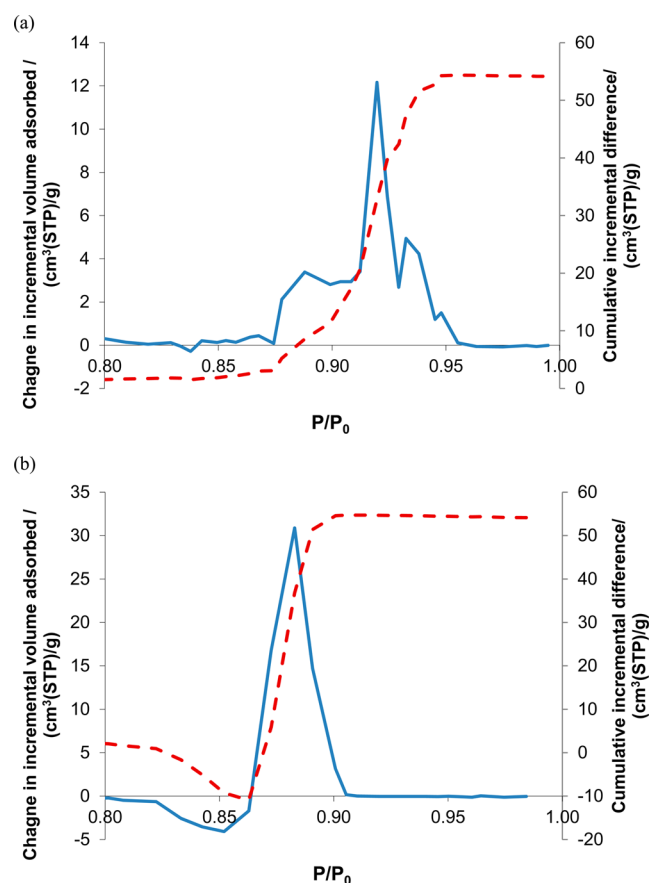


Figure 10. Change in incremental volume adsorbed (between before and after mercury entrapment) plot (solid line; left axis) and cumulative incremental difference plot (dashed line; right axis) for adsorption (a) and desorption (b) of nitrogen on a typical sample from batch E2.

It has been found above that, in the hysteresis loop region of the isotherms, the condensation and evaporation pressures, for argon within a particular subset of the pores that remain accessible after mercury entrapment, increase for the sol-gel silica samples, but not significantly for the alumina sample. The hysteresis width also increases for argon sorption within this subset of pores in silicas. However, corresponding effects of increased relative pressures for condensation and evaporation, and increased hysteresis width, are not observed for nitrogen sorption in any sample. It is noted that it is the same adsorbate-adsorbent systems that have no significant decrease in surface fractal dimension following mercury entrapment that also have a negative peak at high relative pressure in the incremental difference plots. This suggests that, since differences in surface wetting are likely to explain the fractal analysis results for the multilayer region of the isotherms, then a similar explanation probably also applies to the results for the hysteresis region of the isotherm for this subset of still accessible pores which are affected by entrapped mercury. Recent simulation results from Do and co-workers¹⁶ may explain the results for the hysteresis region of the isotherms for this particular subset of pores. It is known that, if the end cross-section of a dead-end pore is made less wetting than the cylindrical-sleeve walls, then the dead-end pore begins to behave like a through pore, in that the width of the sorption hysteresis increases as the adsorption branch position tends toward that expected for a through pore.¹⁶ Further, if dead-end

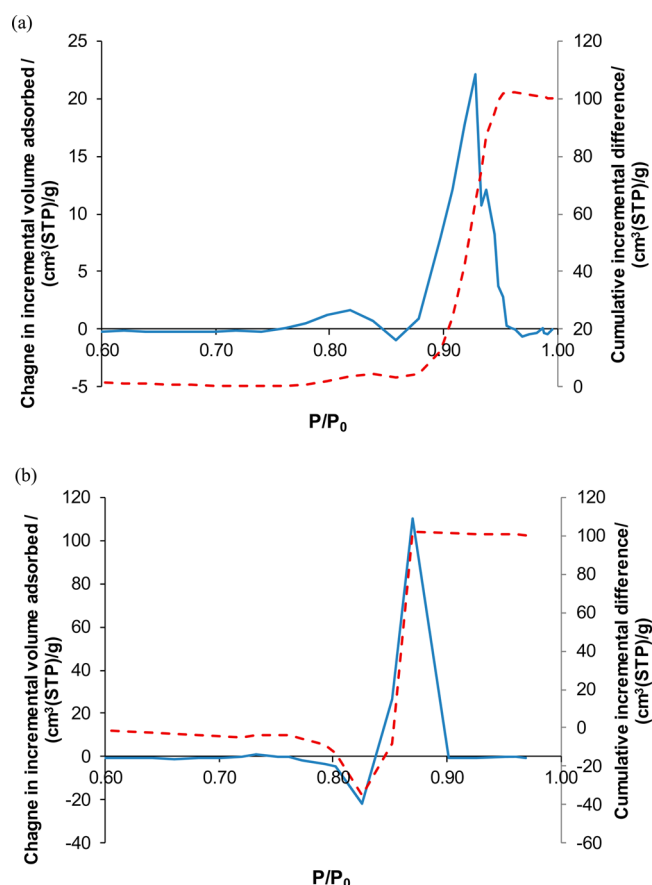


Figure 11. Change in incremental volume adsorbed (between before and after mercury entrapment) plot (solid line; left axis) and cumulative incremental difference plot (dashed line; right axis) for adsorption (a) and desorption (b) of argon on a typical sample from batch E2.

cylindrical pores are shortened, while retaining the same diameter, but are relatively short to begin with, then the relative pressure for condensation and evaporation tends to increase because of the drop in the pore potential.³² Hence, it seems likely that the migration of the relative pressures for adsorption and desorption to higher values, and the increase in hysteresis width, for argon sorption on porous silicas could be caused by a concurrent decline in wetting of the end-wall of a dead-end pore, and a shortening of the pore length, caused by mercury entrapment. This is what might be expected if mercury was to become entrapped as a cylindrical plug at the end wall of a dead-end pore, and argon wetted mercury less than silica. A different result for nitrogen in the same pore system could be obtained if nitrogen wetted mercury to a more similar degree as the silica wall. Given that the Lennard-Jones parameters for mercury are the same as platinum,³³ and the exposed Hg area is ~2–3% of the total surface area, these findings may also have implications for using argon in characterization of supported platinum catalysts.

It has also been found that negative peaks sometimes arise on the low pressure side of the major positive peak in incremental difference plots for desorption data. This means that some pores still accessible after mercury entrapment are desorbing at lower relative pressure than they did before mercury entrapment. This could happen if a large pore body is shielded by necks of (at least) two different, small and medium, sizes. Before mercury entrapment, the route to the surface guarded by

the medium-sized neck might control desorption from the large body. However, if this percolation route becomes blocked by entrapped mercury, then the percolation route for desorption from the large body would then be forced to go through the small-sized neck instead. Hence, desorption at the lower relative pressure corresponding to the smaller neck size would appear to increase after mercury entrapment because it would then also include the additional condensed nitrogen from the large pore body too. Hence, the integrated gas sorption and mercury porosimetry can be used to determine more of the distribution of neck sizes guarding a given pore body size, rather than just being limited to determining the largest critical neck size, as with gas sorption alone.

CONCLUSIONS

It has been found that, while nitrogen is relatively wetting of a heavy metal surface within either a silica or an alumina pore, argon, in contrast, is relatively wetting of a metal surface within an alumina pore, but not in a silica pore. The presence of the heavy metal surface thus leads to a shift to higher pressure in the positions of adsorption and desorption branches, and a widening of the hysteresis, for argon isotherms for nearby pores. Hence, argon adsorption is likely to lead to pore size inaccuracies of ~200% in characterizing silica-supported platinum catalysts. It has also been found that the width of the hysteresis in the silica material is not well modeled by a combination of NLDFT kernels for equilibrium desorption and spinodal condensation. This discrepancy was not due simply to pore-shielding effects on desorption.

AUTHOR INFORMATION

Corresponding Authors

*E-mail: iain.hitchcock@dunelm.org.uk. Tel.: +44 (0)118 924 2253.

*E-mail: sean.rigby@nottingham.ac.uk. Tel.: +44 (0)115 951 4078).

Notes

The authors declare no competing financial interest.

REFERENCES

- (1) Rouquerol, F.; Rouquerol, J.; Sing, K. *Adsorption by Powders and Porous Solids: Principles, Methodology and Applications*; Academic Press: London, 1999.
- (2) Neimark, A. V.; Ravikovitch, P. I. Capillary Condensation in MMS and Pore Structure Characterization. *Microporous Mesoporous Mater.* **2001**, *44*, 697–707.
- (3) Everett, D. H. In *The Solid Gas Interface*; Flood, E. A., Ed.; Marcel Dekker, Inc.: New York, 1967; p 1055.
- (4) Hitchcock, I.; Fletcher, R. S.; Holt, E. M.; Rigby, S. P. Improving Sensitivity and Accuracy of Pore Structural Characterization Using Scanning Curves in Integrated Gas Sorption and Mercury Porosimetry Experiments. *J. Colloid Interface Sci.* **2014**, *417*, 88–99.
- (5) Rigby, S. P.; Fletcher, R. S.; Riley, S. N. Characterization of Porous Solids Using Integrated Nitrogen Sorption and Mercury Porosimetry. *Chem. Eng. Sci.* **2004**, *59*, 41–51.
- (6) Rigby, S. P.; Fletcher, R. S. Experimental Evidence for Pore Blocking as the Mechanism for Nitrogen Sorption Hysteresis in a Mesoporous Material. *J. Phys. Chem. B* **2004**, *108*, 4690–4695.
- (7) Thommes, M.; Smarsly, B.; Groenewolt, M.; Ravikovitch, P. I.; Neimark, A. V. Adsorption Hysteresis of Nitrogen and Argon in Pore Networks and Characterization of Novel Micro- and Mesoporous Silicas. *Langmuir* **2006**, *22*, 756–764.
- (8) Gregg, S. J.; Sing, K. S. W. *Adsorption, Surface Area and Porosity*, 2nd ed.; Academic Press: London, 1982.

- (9) Kruk, M.; Jaroniec, M. Accurate Method for Calculating Mesopore Size Distributions from Argon Adsorption Data at 87 K Developed Using Model MCM-41 Materials. *Chem. Mater.* **2000**, *12*, 222–230.
- (10) Lowell, S.; Shields, J. E.; Thomas, M. A.; Thommes, M. *Characterisation of Porous Solids and Powders: Surface Area, Pore Size and Density*; Spinger: Dordrecht, 2004.
- (11) Barrett, E. P.; Joyner, L. G.; Halenda, P. P. The Determination of Pore Volume and Area Distributions in Porous Substances. I. Computations from Nitrogen Isotherms. *J. Am. Chem. Soc.* **1951**, *73*, 373–380.
- (12) Morishige, K.; Nakamura, Y. Nature of Adsorption and Desorption Branches in Cylindrical Pores. *Langmuir* **2004**, *20*, 4503–4506.
- (13) Oh, J.-G.; Kim, H. Synthesis of Core–Shell Nanoparticles with a Pt Nanoparticle Core and a Silica Shell. *Curr. Appl. Phys.* **2013**, *13*, 130–136.
- (14) Puibasset, J. Grand Potential, Helmholtz Free Energy, and Entropy Calculation in Heterogeneous Cylindrical Pores by the Grand Canonical Monte Carlo Simulation Method. *J. Phys. Chem. B* **2005**, *109*, 480–487.
- (15) Rasmussen, C. J.; Gennady, Y. G.; Neimark, A. V. Monte Carlo Simulation of Cavitation in Pores with Nonwetting Defects. *Langmuir* **2012**, *28*, 4702–4711.
- (16) Nguyen, P. T. M.; Do, D. D.; Nicholson, D. On the Hysteresis Loop of Argon Adsorption in Cylindrical Pores. *J. Phys. Chem. C* **2011**, *115*, 4706–4720.
- (17) Watt-Smith, M. J.; Edler, K. J.; Rigby, S. P. An Experimental Study of Gas Adsorption on Fractal Surfaces. *Langmuir* **2005**, *21*, 2281–2292.
- (18) Matsushashi, H.; Arata, K. Measurement of the Relative Acid Strength and Acid Amount of Solid Acids by Argon Adsorption. *Phys. Chem. Chem. Phys.* **2004**, *6*, 2529–2533.
- (19) Gelb, L.; Gubbins, K. Characterization of Porous Glasses: Simulation Models, Adsorption Isotherms, and the Brunauer–Emmett–Teller Analysis Method. *Langmuir* **1998**, *14*, 2097–2111.
- (20) Androustopoulos, G. P.; Salmas, C. E. A New Model for Capillary Condensation–Evaporation Hysteresis Based on a Random Corrugated Pore Structure Concept: Prediction of Intrinsic Pore Size Distributions. 1. Model Formulation. *Ind. Eng. Chem. Res.* **2000**, *39*, 3747–3763.
- (21) Broekhoff, J. C. P.; De Boer, J. H. Studies on Pore Systems in Catalysts: X. Calculations of Pore Distributions From the Adsorption Branch of Nitrogen Sorption Isotherms in the Case of Open Cylindrical Pores B. Applications. *J. Catal.* **1967**, *9*, 15–27.
- (22) Broekhoff, J. C. P.; De Boer, J. H. Studies on Pore Systems in Catalysts: XIII. Pore Distributions From the Desorption Branch of a Nitrogen Sorption Isotherm in the Case of Cylindrical Pores B. Applications. *J. Catal.* **1968**, *10*, 377–390.
- (23) Pfeiffer, P.; Johnston, G. P.; Deshpande, R.; Smith, D. M.; Hurd, A. J. Structure Analysis of Porous Solids from Preadsorbed Films. *Langmuir* **1991**, *7*, 2833–2843.
- (24) Neimark, A. V.; Hanson, M.; Unger, K. K. Fractal Analysis of the Distribution of High-Viscosity Fluids in Porous Supports. *J. Phys. Chem.* **1993**, *97*, 6011–6015.
- (25) Rigby, S. P.; Chigada, P. I. MF-DFT and Experimental Investigations of the Origins of Hysteresis in Mercury Porosimetry of Silica Materials. *Langmuir* **2010**, *26*, 241–248.
- (26) Fripiat, J. J.; Gatineau, L.; Van Damme, H. Multilayer Physical Adsorption on Fractal Surfaces. *Langmuir* **1986**, *2*, 562–567.
- (27) Mahnke, M.; Mögel, H. J. Fractal Analysis of Physical Adsorption on Material Surfaces. *Colloids Surf., A* **2003**, *216*, 215–228.
- (28) Cohan, L. H. Sorption Hysteresis and the Vapor Pressure of Concave Surfaces. *J. Am. Chem. Soc.* **1938**, *60*, 433–435.
- (29) Porion, P.; Faugère, P.; Levitz, P.; Van Damme, H.; Raoof, A.; Guilbaud, J. P.; Chevoir, F. A NMR Investigation of Adsorption/Desorption Hysteresis in Porous Silica Gels. *Magn. Reson. Imaging* **1998**, *16*, 679–682.
- (30) Perkins, E. L.; Lowe, J. P.; Edler, K. J.; Tanko, N.; Rigby, S. P. Determination of the Percolation Properties and Pore Connectivity for Mesoporous Solids Using NMR Cryodiffusometry. *Chem. Eng. Sci.* **2008**, *63*, 1929–1940.
- (31) Ravikovitch, P. I.; O'Domhnaill, S. C.; Neimark, A. V.; Schuth, F.; Unger, K. K. Capillary Hysteresis in Nanopores: Theoretical and Experimental Studies of Nitrogen Adsorption on MCM-41. *Langmuir* **1995**, *11*, 4765–4772.
- (32) Rigby, S. P.; Chigada, P. I. Interpretation of Integrated Gas Sorption and Mercury Porosimetry Studies of Adsorption in Disordered Networks Using Mean-Field DFT. *Adsorption* **2009**, *15*, 31–41.
- (33) Zhu, S.-B. Interactions of Water, Ions, and Atoms with Metal Surfaces. *Surf. Sci.* **1995**, *329*, 276–284.